DOI: 10.71762/dyhz-qx27

Research Paper

Numerical and Experimental Analysis of Temperature Field, Deformation, and Residual Stress in Two-Stage Single-Pulse Sub-Powder Welding Joints

Hamid Mozafari[1*]
[1]Department of Mechanical Engineering, Faculty of Engineering, Payame Noor University, Tehran, Iran
[*]Email of the Corresponding Author: Mozafari.h@pnu.ac.ir
Received: July 7, 2024; Accepted: August 22, 2024

Abstract
This study investigates the temperature fields, distortion, and distribution of residual stresses in single-pulse sub-powder welding of structural steel. Both experimental and three-dimensional finite element modeling approaches were employed. The heat flux from the welding process was applied as a combination of volumetric and surface heat sources in a Fortran-based program. The indirect coupled method in Abaqus software was utilized for the elastoplastic analysis of the welding process. The dimensions of the molten pool and the heat-affected zone were measured experimentally using metallography and compared with the finite element model. The temperature fields and distortion obtained from the finite element model were also validated against the experimental results. Finally, the influence of constraints on the degree of distortion and residual stresses in the analyzed structure was examined. The comparison of the numerical and experimental results shows good agreement, demonstrating the modeling approach's ability to accurately predict temperature distribution, deformation, and residual stresses in the sub-powder welding process.

Keywords
Submerged arc Welding (SAW), Finite Element Method, Residual Stress, Temperature Distribution

1. Introduction

Welding technology is an increasingly important and versatile field of applied knowledge. Over time, the scope of welding has expanded significantly, encompassing a wide range of areas such as material properties, material resistance, and electrical principles. Compared to other industrial processes, welding stands out as the one with the largest extent and the highest number of interfering parameters. This complexity is a direct result of the critical role welding plays in a variety of industries, including automotive, bridge construction, structural engineering, and pressure vessel manufacturing, among others [1-3]. Given the importance of welded joints in ensuring optimal safety and performance in these industries, considerable efforts have been made to develop methods for accurately measuring and controlling residual stresses. Residual stresses, which are internal stresses that remain in a material even after the external forces have been removed, can significantly impact the structural

integrity and service life of welded components. Consequently, the ability to effectively measure and manage these stresses will be of paramount importance in ensuring the reliability and safety of welded products across a broad spectrum of industrial applications [4].

Residual stresses in welded components arise primarily due to the temperature variations and irreversible deformations that occur during the welding process. When the material is exposed to the intense heat generated at the welding site, thermal stresses develop within the workpiece. Upon completion of the welding operation and removal of the heat source, the material undergoes a significant temperature drop as it cools back down to the ambient temperature. This dramatic change in temperature across the material leads to the formation of residual stresses within the welded part [5]. To better understand and mitigate the impact of these residual stresses, researchers and engineers have turned to numerical simulation techniques. By modeling the welding process using computational methods, it is possible to study the effects of various process parameters on the development of residual stresses and associated distortions. This allows for a deeper understanding of the underlying mechanics and enables the prediction of optimal welding conditions [6].

Through the use of numerical simulations, welding experts can explore how factors such as heat input, welding speed, material properties, and clamping conditions influence the final residual stress state of the welded component. By adjusting these parameters, it becomes feasible to identify the optimal welding conditions that minimize the formation of detrimental residual stresses and distortions. This knowledge can then be applied to improve the overall quality, reliability, and performance of welded structures across a wide range of industrial applications [7].

The analysis of the welding process typically involves two distinct stages. The first step is to determine the spatial and temporal distribution of temperature and heat generated during the welding operation. In the second stage, a mechanical analysis of the process is performed, which allows for the calculation of the distribution of transient thermal stresses and the final residual stress distribution. To model the heat source in the first stage, Goldak presented a mathematical model based on a Gaussian distribution of power density. In his approach, Goldak considered the heat source to be composed of two ellipses. This model offers several key capabilities, including the ability to simulate welding with low or high penetration, asymmetric welding, and the joining of two dissimilar metals. Goldak tested his model by applying it to the welding of two sheets, and the results demonstrated good agreement with experimental values. This indicates that the Goldak heat source model provides a robust and accurate representation of the thermal aspects of the welding process, which is a crucial step in the overall analysis [8].

The stress analysis of the welding process inherently involves a higher degree of complexity and non-linearity compared to the thermal analysis. This is primarily due to the multitude of interdependent variables that come into play when considering the mechanical behavior of the material during and after the welding operation. In the stress analysis stage, the temperature history obtained from the preceding thermal analysis is incorporated as a thermal load into the stress analysis equations. Through this integration, the thermal stresses and strains can be calculated at each time step during the welding process. The final state of residual stress is then determined by the cumulative effect of these thermal stresses and strains that develop throughout the welding cycle [9].

To achieve this, the stress analysis is carried out in a manner that closely aligns with the thermal analysis. Specifically, at each time step, the heat distribution data obtained from the thermal analysis

is applied, and the corresponding thermal stresses are calculated. This step-by-step approach allows for a detailed and accurate representation of the complex thermo-mechanical interactions that occur within the material during welding. By closely coupling the thermal and stress analyses, researchers and engineers can gain a comprehensive understanding of the evolution of residual stresses throughout the welding process. This knowledge is crucial for predicting the long-term performance and reliability of welded structures, as residual stresses can significantly impact the structural integrity and service life of components across a wide range of industries, including automotive, aerospace, and construction [10].

By leveraging the computational power of the finite element method, the researchers were able to develop a detailed numerical model that could accurately predict the thermal and mechanical behavior of the welding process. This approach allowed for a comprehensive analysis of the complex interplay between the temperature fields, distortions, and residual stresses that arise during submerged arc welding [11]. A key aspect of the research was the investigation into the role of constraints on the degree of distortion and residual stress in the welded structure. The researchers systematically examined how the application of various clamping and support conditions during the welding process influenced the final distortion and stress state of the welded component.

In this research study, the finite element method was employed to model the temperature fields and the degree of distortion in submerged arc welding. The simulated results were then compared to the experimental data obtained from laboratory tests, including the measured distortion values and the temporal temperature distribution profiles. Through the combination of numerical simulations and experimental validation, we were able to gain valuable insights into the underlying mechanisms governing the thermo-mechanical behavior of submerged arc welding. This knowledge can inform the development of optimized welding procedures and the design of more reliable and distortion-free welded structures.

2. Materials and Methods

2.1 Experimental work

To measure the temperatures during the welding process at various distances from the welding line, it employed a laser thermometer method. Additionally, the dimensions of the molten pool were determined through metallographic analysis of the welded area, and these measurements were subsequently used as inputs for the numerical simulation. The heat-affected zone was another parameter that was quantified experimentally in this study. The measured values from these experimental techniques were then compared to the results obtained from the numerical simulation conducted using the finite element method.

The laboratory-based portion of the research involved the following steps: selection and preparation of the base metals for the weldment, as well as the consumable electrode, and determination of the welding method. The welding process was then carried out, and the temperature history of the samples was measured using the laser-based method. Finally, a metallographic test was performed to measure the parameters of the molten pool and the dimensions of the heat-affected zone. The material used for the workpiece was ST-37 steel, with a density of 7860 kg/m3. The welding process employed was submerged arc welding, with a heat transfer efficiency (η) of 0.7. The geometric parameters of the sample sheet are depicted in Figure 1.

The measurement of the heat-affected zones was carried out using an infrared thermometer. Thermal infrared imaging cameras are highly sensitive and accurate instruments for measuring infrared radiation, which is emitted and then reflected from the surface of the object being studied. The schematic diagram shown in Figure 2 illustrates the setup and conditions related to the temperature measurement process during the laboratory work.

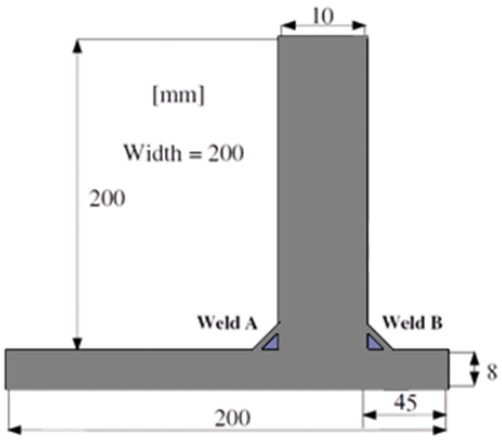

Figure 1. Geometric parameters of the sample sheet

The positions of the measurement locations selected for the study are depicted in the horizontal plane, as shown in Figure 3. This spatial arrangement of the measurement routes provides a comprehensive overview of the temperature distribution and thermal gradients across the welded workpiece. The stress analysis model employed in this research closely followed a bilinear elastoplastic formulation to represent the stress-strain relationship of the material. This approach effectively approximates the actual stress-strain curve of the workpiece material, enabling a more accurate representation of the mechanical behavior during the welding process.

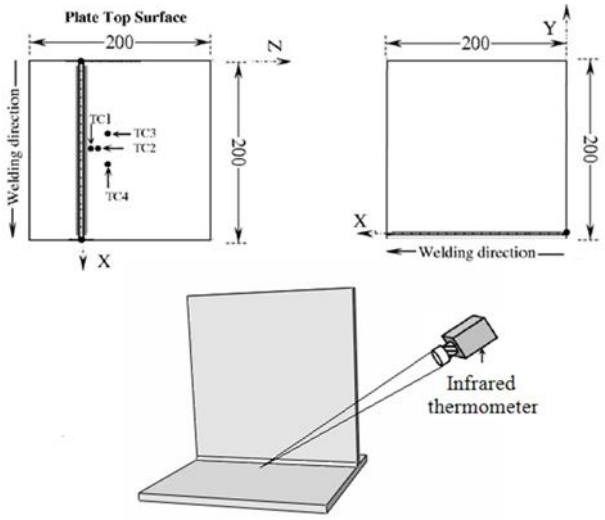

Figure 2. Schematic of temperature measurement scenarios in laboratory work

In addition to the spatial layout of the measurement routes, the specific locations of the temperature measurement points are provided in Table 1. This tabulated data offers a detailed reference for the

precise positions where the temperatures were recorded during the experiments. The inclusion of this information allows for a direct comparison between the experimental measurements and the corresponding results obtained from the numerical simulations. By providing the details on the measurement locations, both in graphical and tabular formats, the researchers have ensured that the experimental setup and data collection procedures are documented. This level of transparency and specificity is crucial for enabling the replication of the study and for facilitating the validation of the numerical modeling approaches employed in the analysis of the welding process.

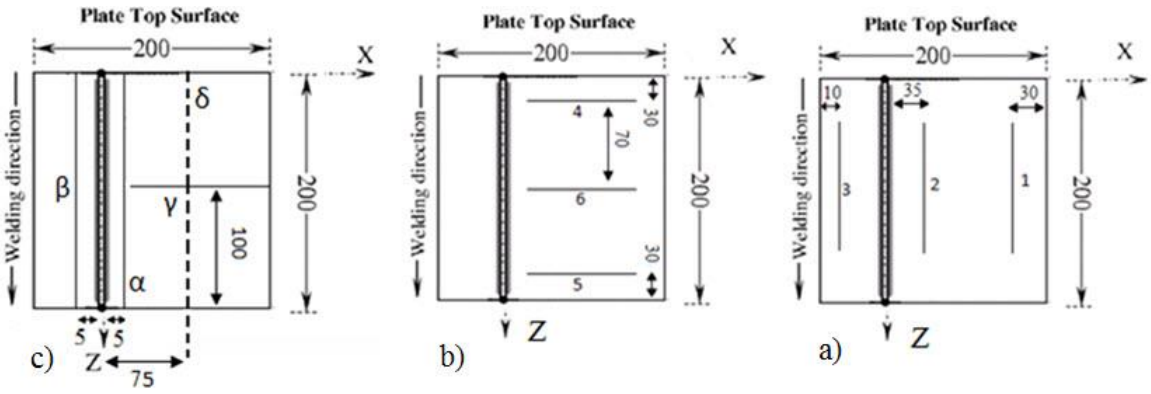

Figure 3. Locations of the selected measurement routes

Table 1. Locations of the temperature measurement points on the samples

	Distance from the beginning of the sheet Z (mm)	Distance from weld line X (mm)
TC1	100	10
TC2	100	13
TC3	90	22
TC4	110	22

The key welding parameters measured for each side of the samples are provided in Table 2. This tabulated data presents the relevant parameters, such as welding current, voltage, and travel speed, which were recorded during the experimental trials .The measurement of the heat-affected zones was conducted using an infrared thermometer. Thermal infrared imaging cameras were employed as the primary tool for this temperature measurement task. These specialized instruments are highly sensitive and accurate in detecting and quantifying infrared radiation. The operating principle of thermal infrared imaging cameras relies on the emission and subsequent reflection of infrared energy from the surface of the object being studied. This non-contact temperature measurement technique allows for the capturing of detailed thermal profiles across the welded workpiece, providing invaluable data for the analysis of the welding process. By combining the tabulated welding parameters with the thermal measurement data obtained from the infrared thermometer and imaging cameras, the researchers were able to develop a comprehensive understanding of the heat generation, distribution, and its impact on the material during the welding process. This holistic dataset serves as a critical input for the numerical simulations and the validation of the computational models.

Table 2. Measured parameters for welding each side of the sample

Steps	Velocity (**mm/s**)	Voltage (V)	Amp (A)	Time (s)
Welding A	5.83	27	310	34.28
Cooling between two pulses	–	–	-	120
Welding A	5.83	27	310	34.28
Final cooling	-	-	-	450

2.2 Modeling the Welding Process

The stress analysis of the welding process is inherently more complex and non-linear compared to the thermal analysis. This increased complexity is primarily due to the higher number of interdependent variables involved in the mechanical behavior of the material during and after the welding operation. In the stress analysis stage, the temperature history obtained from the preceding thermal analysis is incorporated as a thermal load into the stress analysis equations. By doing so, the thermal stresses and strains can be calculated at each time step throughout the welding process. The final state of residual stress is then determined by the cumulative effect of these thermal stresses and strains that accumulate over the course of the welding cycle.

To achieve this, the stress analysis is carried out in a step-by-step manner, where the heat distribution data obtained from the thermal analysis is applied at each time step, and the corresponding thermal stresses are calculated. These stresses are then added to the values calculated in the previous steps, allowing for the simulation of the mechanical behavior of the welding process in a progressive, step-by-step fashion. Figure 4 illustrates the temperature contour at the end of the final cooling stage, as simulated using the Abaqus finite element software. This graphical representation provides a visual depiction of the temperature distribution within the welded workpiece, which is a crucial input for the subsequent stress analysis and the determination of the residual stress state.

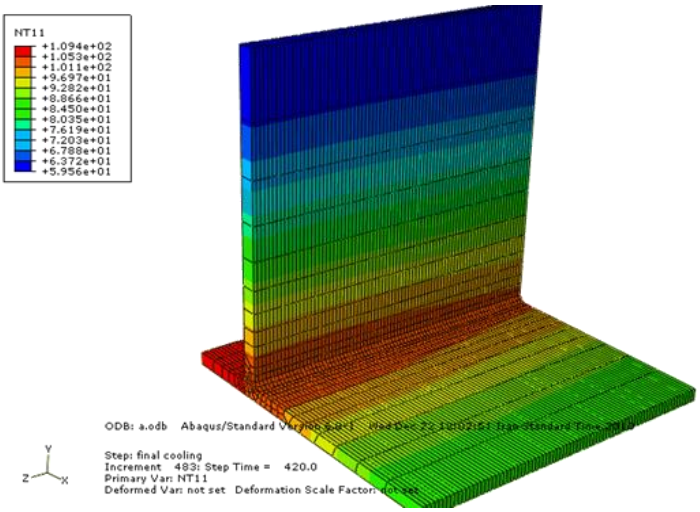

Figure 4. Temperature contour at the end of final cooling

Because the levels of stress and deformation in different regions of the workpiece can vary with changes in the applied boundary conditions, it is possible to optimize the welded component's design and performance based on its intended application. By carefully selecting the appropriate boundary

conditions, it is feasible to identify the areas within the workpiece that experience the highest levels of stress or the greatest degree of deformation. This knowledge can then be used to ensure that the critical regions of the welded part are designed to withstand the anticipated loads and operational conditions with minimal adverse effects from residual stresses or welding-induced deformations.

To facilitate the application of the desired boundary conditions, the relevant planes of the workpiece have been numbered from 1 to 5, as depicted in Figure 5 and tabulated in Table 3. This systematic labeling and documentation of the boundary condition application points provide a clear reference for the subsequent analysis and optimization of the welded component's performance.

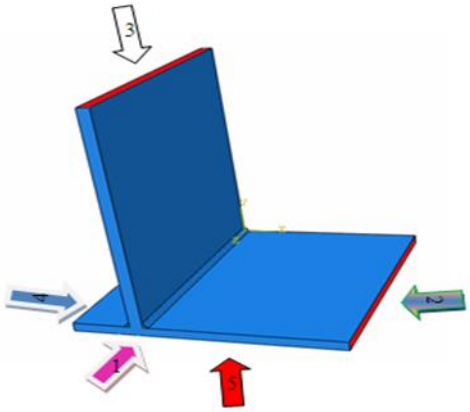

Figure 5. Pages 1 to 5 bound in different x, y, z directions

Table 3. Different binding modes for pages 1-5 in x, y, and z directions

	Page 1	Page 2	Page 3	Page 4	Page 5
A	$U_{x=0},u_{y=0}$	-	$U_{x=0},u_{y=0},u_{z=0}$	$U_{x=0},u_{y=0},u_{z=0}$	-
B	$U_{x=0},u_{y=0}$	-	$u_{y=0}$	$U_{x=0},u_{y=0},u_{z=0}$	-
C	$U_{x=0},u_{y=0},u_{z=0}$	-	$U_{x=0},u_{y=0},u_{z=0}$	$U_{x=0},u_{y=0},u_{z=0}$	-
D	$u_{y=0}$, $u_{z=0}$	-	$u_{y=0}$	$U_{x=0},u_{y=0},u_{z=0}$	-
E	$U_{x=0}$	$U_{x=0},u_{y=0},u_{z=0}$	$U_{x=0},u_{y=0},u_{z=0}$	-	-
F	$U_{x=0}$	$u_{y=0}$	$U_{x=0},u_{y=0},u_{z=0}$	$u_{y=0}$	-
G	$U_{x=0}$	$u_{z=0}$	$u_{y=0}$	-	$u_{y=0}$
H	$U_{x=0}$	$u_{z=0}$	$u_{y=0}$	-	-
I	$U_{x=0}$	-	$U_{x=0},u_{y=0},u_{z=0}$	$U_{x=0},u_{y=0},u_{z=0}$	-
J	$U_{x=0}$	-	$U_{x=0},u_{y=0},u_{z=0}$	-	-
K	$U_{x=0},u_{y=0},u_{z=0}$	$u_{y=0},u_{z=0}$	$u_{y=0}$	-	$u_{y=0}$
L	$U_{x=0},u_{y=0},u_{z=0}$	$u_{y=0}$, $u_{z=0}$	$u_{y=0}$	-	-
M	$U_{x=0},u_{y=0},u_{z=0}$	$u_{z=0}$	$u_{y=0}$	-	$u_{y=0}$
N	$U_{x=0},u_{y=0},u_{z=0}$	$u_{z=0}$	$u_{y=0}$	-	-
O	-	$U_{x=0},u_{y=0},u_{z=0}$	-	-	-
P	-	-	$U_{x=0},u_{y=0},u_{z=0}$	$U_{x=0},u_{y=0},u_{z=0}$	-
Q	$U_{x=0}$	-	-	-	-
R	$u_{y=0}$ $U_{x=0,}$	-	-	-	-
S	$U_{x=0},u_{y=0},u_{z=0}$	-	-	-	-

2.3 Numerical Analysis

The heat transfer phenomenon during welding is a time-dependent (transient) problem, and therefore, the time-dependent heat transfer equations are employed to analyze this process. In general, the heat

transfer in metals is governed by Fourier's law, which states that the heat flux per unit area is proportional to the temperature gradient, with the thermal conductivity being the proportionality coefficient:

$$q = -k_n \frac{\partial T}{\partial n} \tag{1}$$

This heat flux is directed perpendicular to the surface. By combining Fourier's law and the principle of conservation of energy, the heat equation can be derived, which is independent of any strain effects:

$$\rho c \frac{\partial T}{\partial t} = \nabla.(k\ \nabla T) + \dot{Q} \tag{2}$$

Where ρ is the material density, c is the specific heat capacity, T is the temperature, t is the time and $\dot{Q}$ represents any internal heat generation or volumetric heat sources. This heat equation forms the basis for the numerical analysis of the transient heat transfer during the welding process. Additionally, the power density distribution within the front quadrant of the weld can be expressed as a relationship, as shown in Equation (3).

$$q_f(x,y,z,t) = \frac{6\sqrt{3} f_f Q}{abc_f \pi\sqrt{\pi}} e^{-3x^2}/a^2 e^{-3y^2}/b^2 e^{-3[z+v(\tau-t)]^{-2}}/{c_f}^2 \tag{3}$$

Similarly, the power density distribution inside the rear quadrant is defined as equation (4):

$$q_f(x,y,z,t) = \frac{6\sqrt{3} f_f Q}{abc_r \pi\sqrt{\pi}} e^{-3x^2}/a^2 e^{-3y^2}/b^2 e^{-3[z+v(\tau-t)]^{-2}}/{c_r}^2 \tag{4}$$

$$f_f = \frac{2c_f}{c_f + c_r} \qquad\qquad f_r = \frac{2c_r}{c_f + c_r}$$

The heat equation is a second-order partial differential equation for the spatial coordinates, which means that two boundary conditions are required for each coordinate to fully describe the system. However, since the equation is of the first degree for time, only one initial condition is necessary. Several common boundary conditions are typically used in thermal problems, and these can be expressed mathematically. These boundary conditions are applied at the material surface, where heat transfer occurs. One such boundary condition is the constant surface temperature, also known as the Dirichlet condition. This condition provides a suitable approximation when the surface is in contact with a melting solid or a boiling liquid, as the temperature at the surface remains constant.

The mathematical representation of the constant surface temperature boundary condition is as follows:

$$T(0,t) = T_s \tag{5}$$

T_s is the constant surface temperature. This type of boundary condition is particularly useful in scenarios where the surface temperature is well-defined, such as in cases where the workpiece is in direct contact with a heat source or a cooling medium with a known temperature.

The second boundary condition is the specified heat flux, also known as the Neumann condition. This condition may be applicable when an electric heating plate is connected to the surface. The mathematical representation of the specified heat flux boundary condition is:

$$-k\left.\frac{\partial T}{\partial X}\right|_{X=\cdot} = q_s \tag{6}$$

Where q_s is the constant heat flux on the surface. The third boundary condition is the insulation or adiabatic condition, which is a special case of the Neumann condition where the heat flux at the surface is zero:

$$\left.\frac{\partial T}{\partial X}\right|_{X=\cdot} = \cdot \tag{7}$$

The fourth boundary condition is the convective heat transfer at the surface, which follows Newton's law of cooling:

$$-k\left.\frac{\partial T}{\partial X}\right|_{X=\cdot} = h_c\left(T_s - T_\infty\right) \tag{8}$$

Here, T_s is the temperature of the fluid in contact with the surface, T_∞ is the surface temperature, and h_c is the heat transfer coefficient, which is a function of the fluid properties, surface geometry, and flow conditions. The fifth boundary condition is the radiative heat transfer at the surface, which can be calculated using Stefan Boltzmann's law:

$$-k\left.\frac{\partial T}{\partial X}\right|_{X=\cdot} = \varepsilon\sigma_{sb}(T_s^{۴} - T_{sur}^{۴}) \tag{9}$$

Where

T_{sur} is the temperature of the surrounding environment

ε is the emission coefficient of the body

and σ_{sb} is Stefan Boltzmann's constant, whose value is equal to $5.67*10^{-8}$ $k/m.^2K^4$.

3. Results and Discussion

The characterization of the Goldak double-ellipsoidal heat source model is a crucial step in the numerical modeling of the welding process. This heat source model is widely used to simulate the transient temperature field during welding operations, as it can accurately capture the complex thermal distribution within the weld pool and the surrounding region. In the context of the present study, the experimental determination of the Goldak model parameters was carried out for the submerged arc welding (SAW) process. Figure 6 illustrates the measurement procedure for parameters *a* and *b*, which define the dimensions of the front and rear ellipsoids of the heat source, respectively.

Additionally, Figure 7 shows the experimental measurement of the c_f and c_r parameters, which represent the penetration depths of the front and rear ellipsoids, respectively. These parameters are essential in accurately describing the heat input distribution and the resulting thermal history within the welded workpiece. The careful characterization of the Goldak model parameters is crucial, as they directly influence the predicted temperature field, thermal gradients, and ultimately, the resulting microstructure and mechanical properties of the welded joint. By incorporating the experimentally determined Goldak model parameters into the numerical simulations, the computational model can be calibrated to accurately capture the welding thermal history, which is a prerequisite for further analyses, such as the evaluation of residual stresses, distortion, and phase transformations.

The thermal history during the submerged arc welding (SAW) process is a critical factor in determining the resulting microstructure and mechanical properties of the welded joint. Figure 8 (a, b, c, and d) presents the temperature-time curves obtained at various locations within the workpiece, specifically at distances of 10 mm, 13 mm, and 22 mm from the welding centerline, and at a distance of 22 mm from the start of the weld. The experimental temperature measurements, obtained through laboratory testing, are compared to the numerical simulation results from the finite element analysis. This comparison demonstrates the ability of the computational model to accurately capture the transient temperature evolution during the welding process.

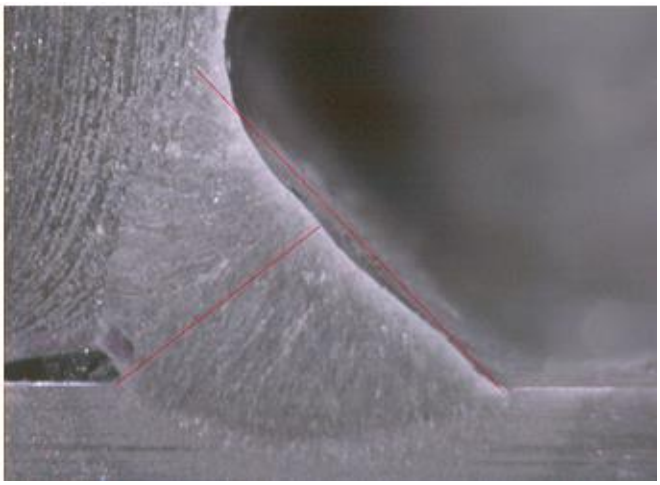

Figure 6. Measurement of parameters *a* and *b* of the Goldak thermal model in welding

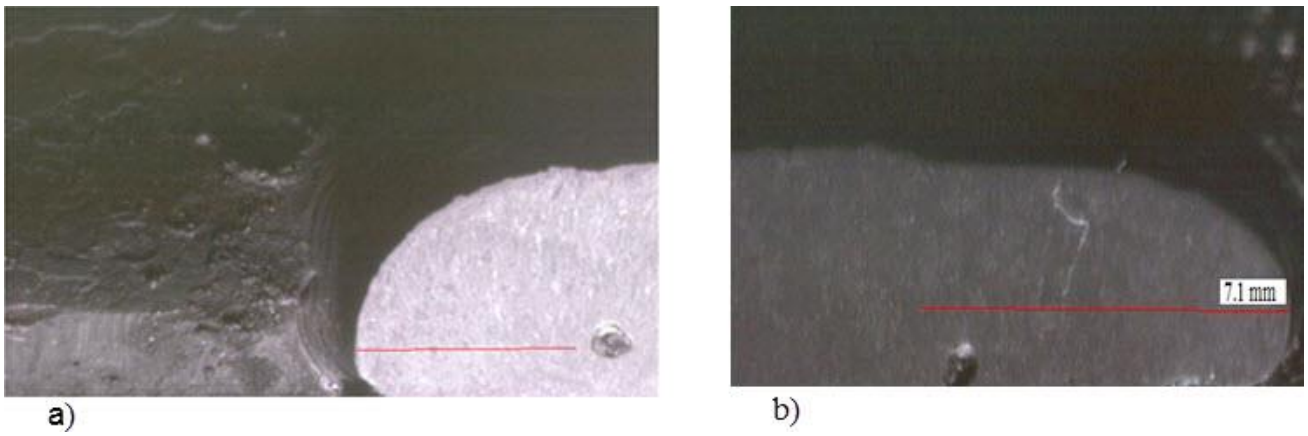

Figure 7. Measurement of Goldak thermal model parameters in the welded sample, a) c_f, b) c_r

The slope of the temperature-time curves represents the cooling rate, which is a crucial parameter governing the microstructural development and the resulting mechanical properties of the welded joint. The good agreement between the experimental and numerical cooling rates, as observed in most regions, validates the thermal modeling approach and the incorporation of the Goldak heat source parameters determined in the earlier characterization step. The distinct temperature peaks observed in the curves correspond to the moment when the heat source (the welding arc) passes through the respective measurement locations. As the heat source moves away, the temperature gradually decreases and approaches the ambient temperature. From these temperature-time curves, not only the peak temperatures but also the cooling rates can be extracted, providing valuable insights into the thermal history experienced by the workpiece during the welding process.

The distortion of the welded workpiece is a critical consideration in the assessment of the welding process performance. In the present study, the out-of-plane deformation of the horizontal plane along the y-axis was investigated in detail. As shown in Figure 3(a,b), six different measurement directions were considered to capture the spatial variation of the distortion profile. Figures 9(a) through 9(f) present the displacement diagrams obtained from the finite element analysis of the submerged arc welding (SAW) process. These numerical results provide valuable insights into the magnitude and distribution of the out-of-plane deformation experienced by the workpiece.

Based on the displacement curves depicted in Figures 9(a-f), it can be observed that the maximum value of the sheet displacement, under the specified boundary conditions for the SAW process, is approximately 4.6 mm. This quantitative information is essential for evaluating the overall deformation behavior of the welded structure and determining the necessary corrective measures, such as the application of clamping fixtures or the optimization of welding parameters, to mitigate the detrimental effects of distortion. The careful analysis of the distortion profiles along multiple directions provides a comprehensive understanding of the three-dimensional deformation patterns induced by the welding process. This level of detail is crucial for the accurate prediction of residual stresses, which are closely linked to the observed distortion. By integrating the numerical simulation results with the experimental measurements, the welding process can be better understood, and strategies can be developed to control and minimize the undesirable distortion of the welded structures.

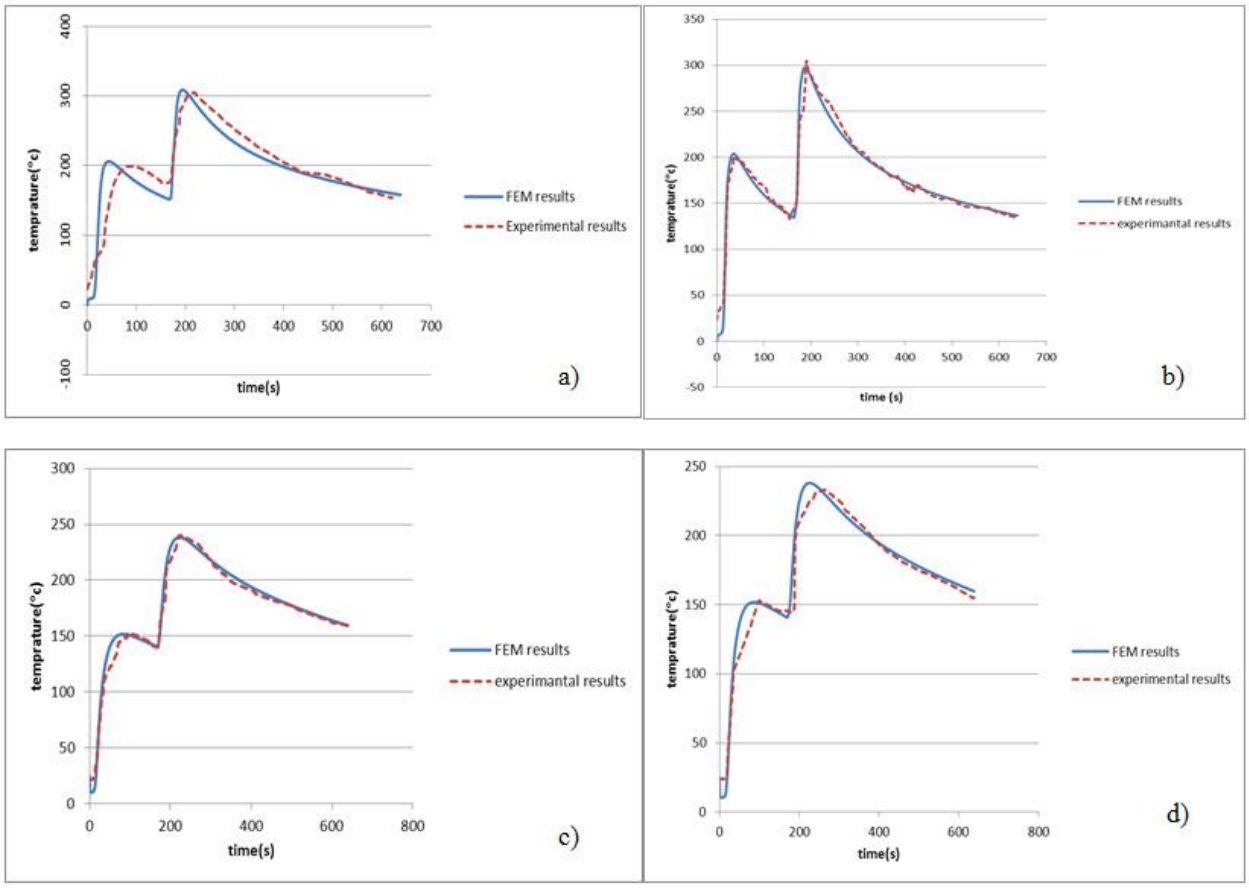

Figure 8. Temperature curves over time using the sub-powder method, a) 10 *mm* from welding line (TC1), b) 13 *mm* from welding line (TC2), c) 22 *mm* from welding line (TC3), d) 22 *mm* from welding line (TC4)

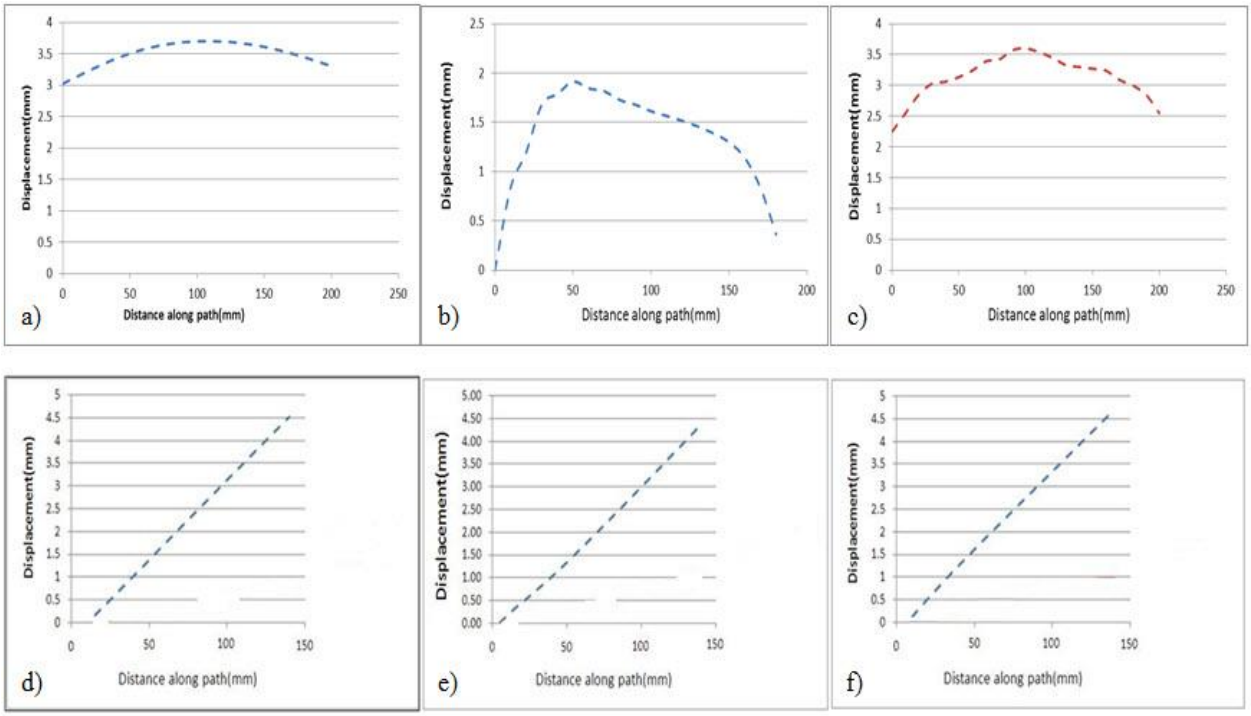

Figure 9. Diagrams of location change along the sheet length using the sub-powder method, a) line 1, b) line 2, c) line 3, d) line 4, e) line 5, f) line 6

The numerical stress analysis in the present study employed a bilinear elastoplastic material model, which provides a realistic representation of the stress-strain behavior of the workpiece material. As shown in Figure 3(c), several measurement paths were selected on the horizontal plane to evaluate the distribution of the residual stresses. Figure 10(a) presents the transverse residual stress (σ_{xx}) profile along the α line on the welded sheet. This diagram reveals that the maximum tensile residual stress in the x-direction is approximately 200 MPa, located at the end of the weld. Towards the beginning of the weld, the tensile residual stress decreases to around 80 MPa. Interestingly, in the areas closer to the sheet edges, compressive residual stresses are observed, which is necessary to satisfy the overall equilibrium conditions.

By closely examining the displacement diagrams in Figures 9(b) and 8(c), and the residual stress plot in Figure 10(b), an insightful correlation can be made. At the end of the weld, where the workpiece experiences relatively lower levels of out-of-plane deformation, the residual stresses are higher in magnitude. Conversely, towards the initial edge of the weld, the decreased residual stresses correspond to the larger displacement and distortion observed in that region. This inverse relationship between the residual stresses and the distortion patterns highlights the complex interplay between the thermal history, mechanical deformation, and the resulting stress fields within the welded structure. The detailed analysis of these interdependent phenomena is crucial for predicting and controlling the final state of the welded component, including the potential for crack initiation, stress-induced distortion, and overall structural integrity.

The residual stress analysis in the welded structure also considered the longitudinal stress component (σ_{zz}) along the α direction, as depicted in Figure 10(c). This diagram reveals that the longitudinal residual stresses are more critical towards the end regions of the weld. However, the maximum value of the longitudinal residual stress is lower than the peak transverse residual stress observed earlier.

Interestingly, the longitudinal stress in the middle regions of the weld is slightly higher than the corresponding transverse stress. Figure 10(c) also presents the transverse residual stress (σ_{xx}) distribution along the α line on the bottom surface of the horizontal workpiece. The maximum compressive residual stress at the beginning of the weld is approximately 80 MPa, while the maximum tensile residual stress at the end of the weld is also around 80 MPa. Notably, the residual stresses in the middle regions of the weld are relatively low.

The residual stress profile along the β path, as shown in Figure 10(d), exhibits a similar trend to the α path, but with slightly lower overall stress magnitudes. This observation can be attributed to the increased out-of-plane deformation observed in the regions closer to the β line, as compared to the areas near the α line. The higher distortion in the β region leads to a redistribution of the residual stresses, resulting in the observed differences between the two paths.

Figure 11(a) presents the transverse residual stress (σ_{xx}) along the γ line, where the stresses are tensile near the weld centerline and gradually transition to compressive stresses at locations further away from the weld. Additionally, Figure 11(b) indicates that a significant portion of the workpiece experiences compressive longitudinal residual stresses (σ_{zz}). The distortion of the welded workpiece is further analyzed by examining the out-of-plane displacement along the y-axis, specifically in the γ and δ directions, as shown in Figures 11(a) and 11(b), respectively. Figure 11(a) depicts the displacement profile along the γ direction. It can be observed that as the measurement location approaches the edge of the sheet, the overall distortion increases. This is attributed to the angular twist of the workpiece, which becomes more pronounced towards the free edges. The slope of the displacement curve in the γ direction gradually decreases as one moves away from the weld centerline, indicating a reduction in the angular twist.

This behavior can be explained by the localized nature of the welding-induced distortion. The regions closer to the weld centerline experience the highest thermal gradients and associated mechanical deformations, leading to the development of significant angular twists. However, as the distance from the weld increases, the angular twist and the associated out-of-plane displacement diminish, as the workpiece tends to approach a more planar configuration away from the primary source of the distortion, which is the welding heat input. The observed trends in the distortion profiles along the γ and δ directions provide valuable information for understanding the three-dimensional deformation patterns induced by the welding process. This knowledge is crucial for the development of effective distortion mitigation strategies, such as the optimization of welding parameters, the use of appropriate clamping fixtures, or the application of post-weld treatments, to ensure the dimensional accuracy and structural integrity of the final welded assembly.

The residual stresses and distortion in a welded structure are strongly influenced by the applied boundary conditions, which can vary depending on the intended application and service conditions of the welded component. By carefully considering the constraints and support conditions during the welding process, it is possible to tailor the residual stress and deformation profiles to minimize their adverse effects on the part's performance and reliability. The present study investigates the influence of different boundary condition scenarios on the resulting stress and deformation fields within the welded structure. Figures 12 through 15 show the stress profiles along the α, β, γ, and δ paths, respectively, under various constraint conditions.

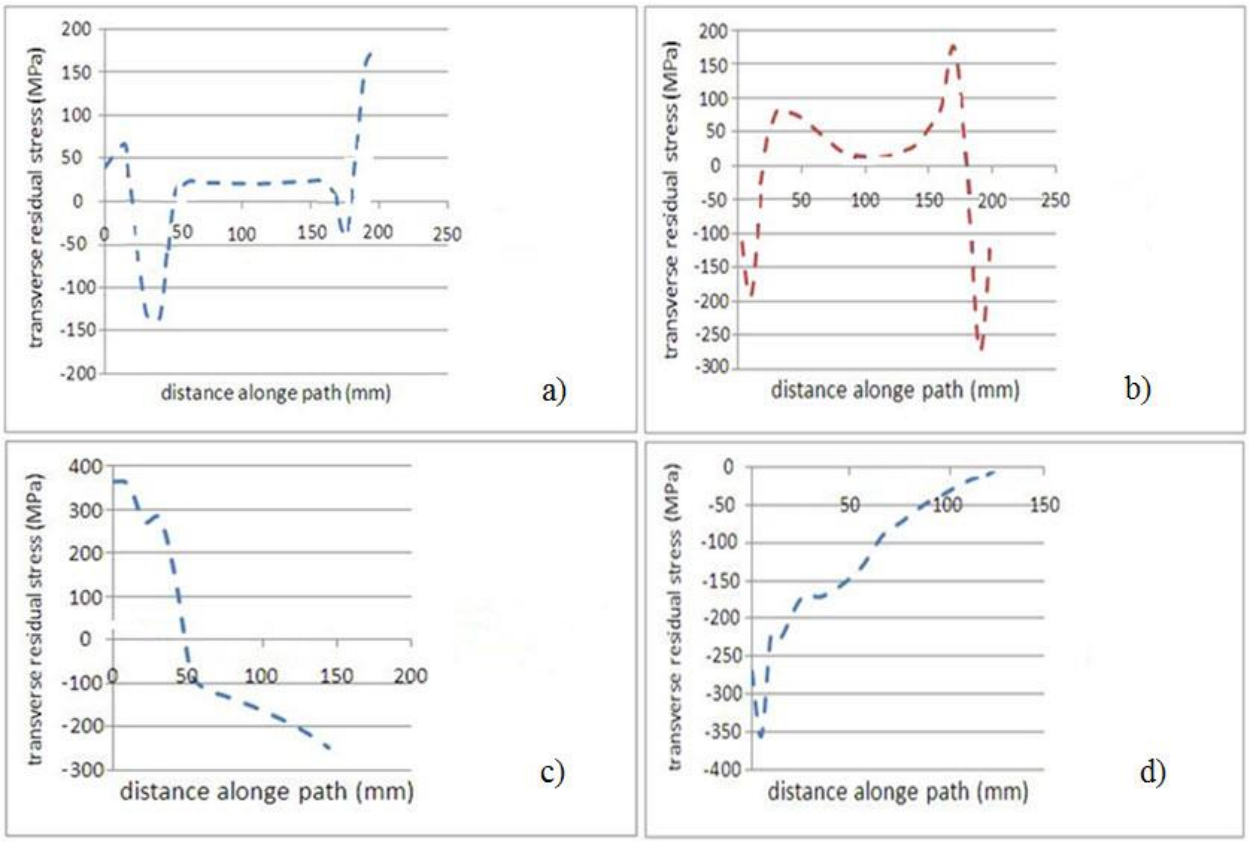

Figure 10. Diagrams of residual stresses a) transverse along line α under the sheet, b) transverse along line β on the sheet, c) transverse along line γ on the sheet, d) longitudinal along line γ on the sheet

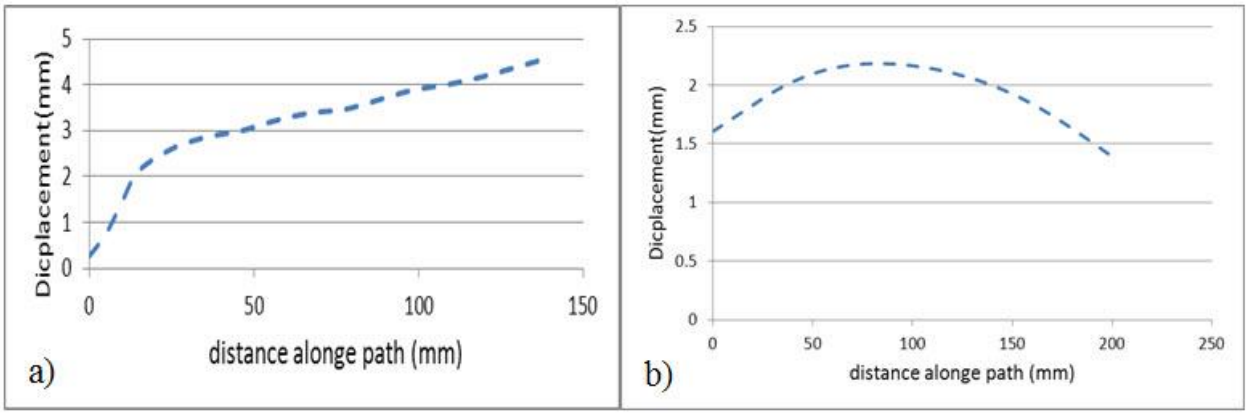

Figure 11. Changing the horizontal sheet location in a) γ direction, b) δ direction

Figure 12 reveals that the maximum out-of-plane displacement is observed along the mok path. Interestingly, some regions exhibit positive displacement, while others experience negative (downward) displacement. This indicates the presence of complex three-dimensional deformation patterns within the welded workpiece, which can be attributed to the localized thermal gradients and the resulting non-uniform expansion and contraction of the material. By adjusting the boundary conditions, the residual stress and distortion distributions can be actively managed to ensure the optimal performance of the welded structure during service. For instance, the placement of strategic

clamping or support points can help minimize the critical stress concentrations and reduce the overall deformation of the component.

Furthermore, the understanding of the stress and deformation behavior under various boundary condition scenarios provides valuable insights for the selection of the most appropriate application and usage of the welded part. Regions with lower residual stresses and distortion can be identified as the most suitable locations for the critical functional components, while areas with higher stress and deformation can be avoided or reinforced as necessary.

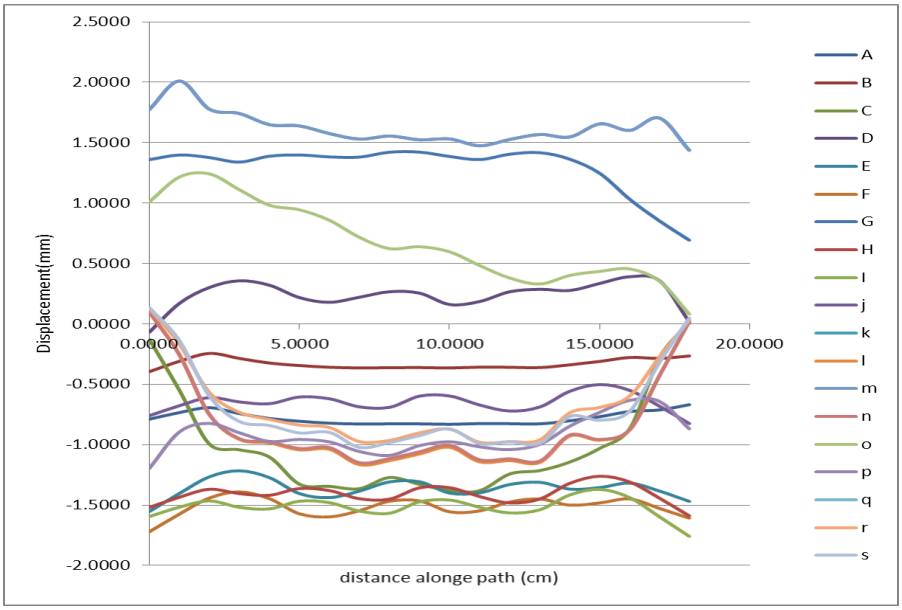

Figure 12. Deformation of the sheet in the α direction under different fixation states from A to S

Figure 13 presents the out-of-plane deformation of the welded sheet along the β direction under different boundary condition scenarios. For the state I constraint configuration, the maximum observed displacement is approximately 3.4 mm. Interestingly, the displacement profiles exhibit both positive and negative values, indicating the occurrence of complex three-dimensional distortion patterns within the welded structure. The presence of both upward and downward displacement components along the β path highlights the complex nature of the welding-induced deformation. This behavior can be attributed to the non-uniform thermal history and the associated uneven thermal expansion and contraction of the material during the welding process.

The detailed analysis of the deformation profiles along the β direction provides valuable insights into the overall distortion characteristics of the welded component. By understanding the magnitude and direction of the displacements, engineers can better predict the potential impact on the structural integrity, dimensional accuracy, and functional performance of the welded assembly. Furthermore, the observation of both positive and negative displacement components suggests the need for a comprehensive three-dimensional approach to the analysis and mitigation of welding-induced distortion. Simplistic assumptions of uniform or one-dimensional deformation may overlook critical aspects of the problem, leading to inaccurate predictions and suboptimal distortion control strategies.

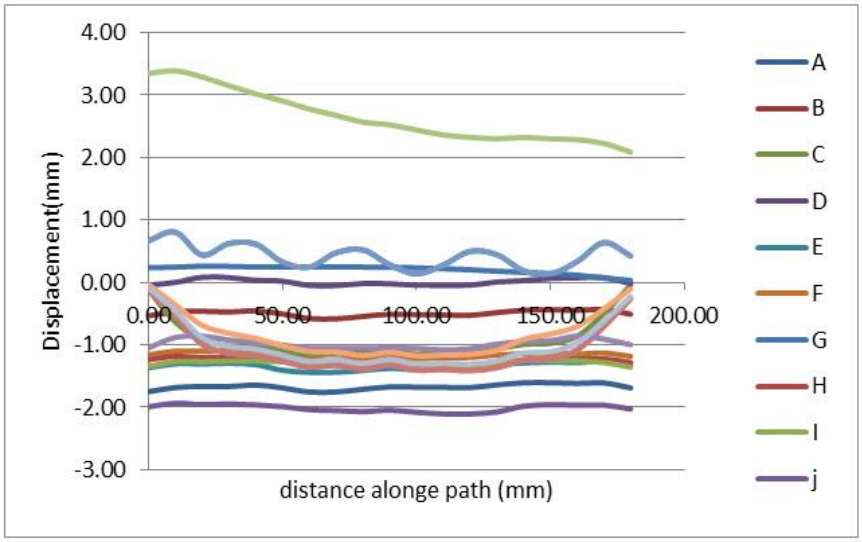

Figure 13. Deformation of the sheet in the β direction under different fixation states from A to S

The highest residual stress is observed in the fixation mode 'm', where the first plate is constrained in the u_1, u_2, and u_3 directions, the second plate is constrained in the u_3 direction, and the third plate is constrained in the u_2 direction. Under this scenario, the maximum residual stress reaches approximately 350 MPa. The peak residual stress values and their overall behavioral trends are generally similar across the different fixation modes, with no significant deviations. However, there are notable differences between the stress states. The highest residual stress is associated with the *k* and *m* fixation mode, while the lowest is observed in the *c* fixation mode. The difference in the peak residual stress between these two scenarios can reach up to 300 MPa. Except for the regions near the edges, the residual stress values are relatively close to each other under the various constraint conditions.

Figure 14 presents the out-of-plane displacement profiles along the γ path, which originates from the midpoint of the weld line and extends towards the free end of the workpiece. This displacement analysis provides valuable insights into the spatial distribution of the welding-induced distortion. The observed displacement trends indicate that the regions closer to the weld centerline experience relatively lower out-of-plane deformation, while the displacement magnitudes increase progressively towards the free edges of the workpiece. This behavior can be attributed to the localized nature of the thermal gradients and the associated uneven expansion and contraction of the material during the welding process.

The highest out-of-plane displacement is observed for the *j* constraint scenario, particularly at the free end of the workpiece, furthest from the weld line. Conversely, the *g* constraint configuration exhibits the lowest displacement values along the γ path. The variation in the displacement magnitudes along the γ path can be explained by the influence of the boundary conditions on the overall deformation behavior of the welded structure. The different constraint modes alter the stress distribution and the resulting out-of-plane distortion patterns within the component.

By understanding the relationship between the boundary conditions, the weld location, and the resulting deformation profiles, engineers can develop strategies to mitigate the adverse effects of welding-induced distortion. This may involve the optimization of clamping or support arrangements,

the adjustment of welding parameters, or the incorporation of post-weld treatments to introduce beneficial compressive residual stresses and counteract the distortion.

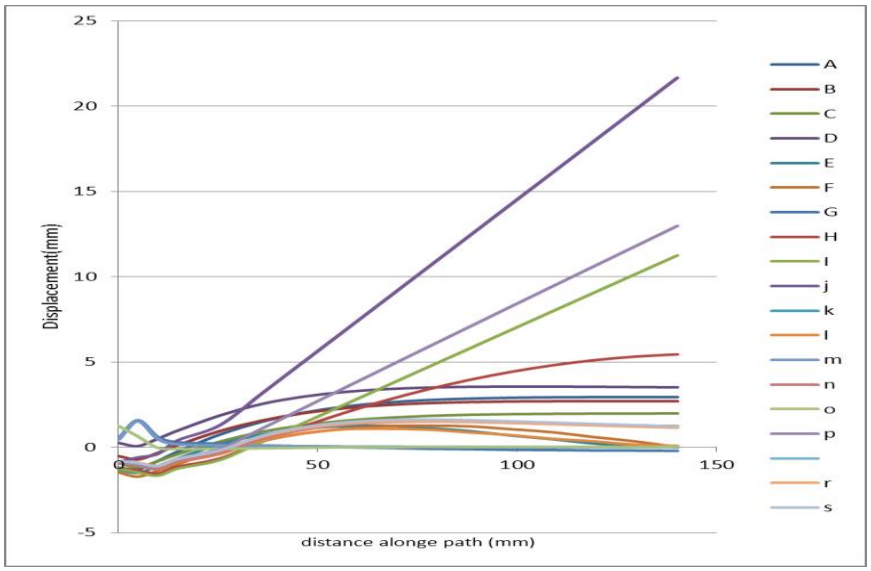

Figure 14. Deformation of the sheet in the γ direction under different fixation states from A to S

Figure 15 presents the out-of-plane displacement profile along the δ path within the welded workpiece. Similar to the trends observed for the γ path, the displacement magnitudes along the δ direction also exhibit a strong dependence on the applied boundary conditions. The highest out-of-plane deformation is associated with the *j* constraint scenario, where the displacement reaches its peak value along the δ path. Conversely, the *g* constraint configuration results in the lowest displacement magnitudes among the examined cases.

The observed differences in displacement behavior along the δ path can be attributed to the complex interplay between the thermal gradients induced by the welding process and the imposed boundary conditions. The *j* constraint mode, which likely involves fewer support points or less rigid fixation, allows for a greater degree of freedom for the material to deform under welding-induced thermal stresses. This, in turn, leads to the amplification of the out-of-plane distortion along the δ path. On the other hand, the *g* constraint scenario, with its more restrictive boundary conditions, effectively limits the deformation of the welded structure, resulting in the observed lower displacement values along the δ path. The understanding of displacement behavior along critical paths, such as the δ direction, is crucial for the development of effective distortion mitigation strategies. By identifying the boundary condition scenarios that lead to the highest deformation, engineers can focus their efforts on optimizing the support and clamping arrangements, the welding parameters, or the application of post-weld treatments to minimize the adverse effects of welding-induced distortion.

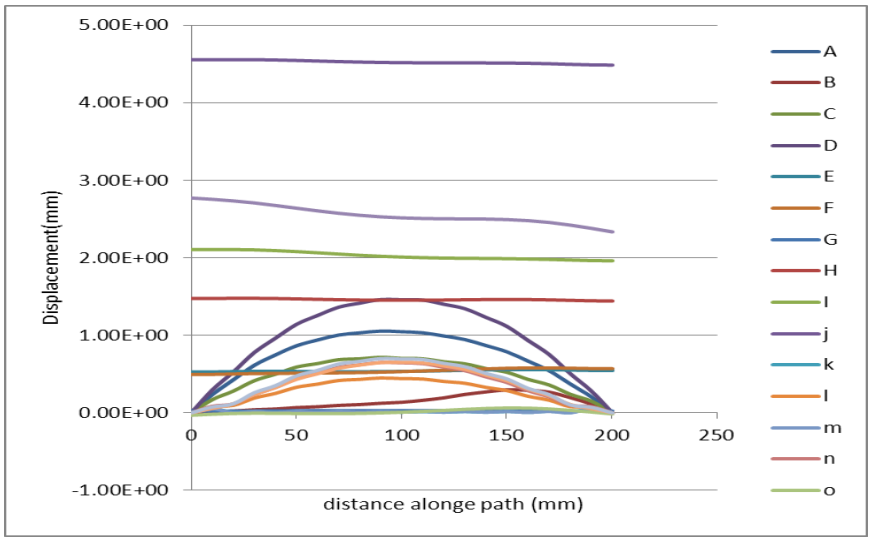

Figure 15. Deformation of the sheet along path δ under different fixation states from A to S

4. Conclusion

This study presents a comprehensive numerical and experimental investigation into the thermal, deformation, and residual stress characteristics of two-stage single-pulse submerged arc welding (SAW) joints. The numerical analysis was conducted using a finite element approach implemented in the Abaqus software. The model closely represented the actual welding process, including the dimensions, material properties, joint configuration, and heat source parameters. The thermal and mechanical aspects of the welding process were both incorporated into the finite element analysis. To validate the numerical model, the researchers conducted experimental measurements, using thermocouples installed on the workpiece to record the temperature evolution during the welding process. The excellent agreement between the numerical predictions and the experimental data demonstrated the accuracy and reliability of the developed finite element model in capturing the key characteristics of the SAW process. The successful validation of the thermal model provides confidence in the ability of the numerical approach to accurately predict the temperature fields and the associated thermal histories within the welded joint. This is a critical step, as the thermal profiles directly govern the development of residual stresses and distortion within the welded structure.

Furthermore, the validated finite element model can be effectively employed to investigate the influence of various process parameters, material properties, and boundary conditions on the resulting temperature distributions, residual stress states, and deformation patterns. This capability enables the optimization of the SAW process to minimize the adverse effects of welding-induced defects and ensure the dimensional accuracy and structural integrity of the final welded assembly.

5. References

[1] Hassanifard, S., Nabavi-Kivi, A., Ghiasvand, A. and Varvani-Farahani, A. 2021. Monotonic and fatigue response of heat-treated friction stir welded Al 6061-T6 joints: Testing and characterization. Materials Performance and Characterization. 10(1):353-369. doi: 10.1520/MPC20200076.

[2] Yaghi A., Hyde T. H., Becker A. A., Sun W. and Williams J. A. 2006. Residual stress simulation in thin and thick-walled stainless steel pipe welds including pipe diameter effects. International Journal of Pressure Vessels and Piping. 83(11): 864-874. doi:10.1016/j.ijpvp.2006.08.014.

[3] Li, J.Q. and Liu, H.J. 2015. Effects of the reversely rotating assisted shoulder on microstructures during the reverse dual-rotation friction stir welding. Journal of Materials Science & Technology. 31(4):375-383. doi:10.1016/j.jmst.2014.07.020.

[4] Liu, H.J., Li, J.Q. and Duan, W.J. 2013. Research on reverse dual rotation friction stir welding process. In Proceedings of the 1st international joint symposium on joining and welding. Woodhead Publishing, 25-32. doi:10.1533/978-1-78242-164-1.25.

[5] Sun, L., Ren, X. and Hi, J., 2021. Numerical investigation of a novel pattern for reducing residual stress in metal additive manufacturing. Journal of Materials Science & Technology. 67:11-22. doi:10.1016/j.jmst.2020.05.080.

[6] Thomas, W.M., Staines, D.J., Watts, E.R. and Norris, I.M. 2005. The simultaneous use of two or more friction stir welding tools. Abington, Cambridge, TWI published on the Internet.

[7] Nakhodchi, S. Akbari, S., Shokufar A. and Rezazadeh, H. 2014. Numerical and experimental study of temperature and residual stress in multi-pass welding of two stainless steel plates having different thicknesses. 14(9):81-89. doi: 20.1001.1.10275940.1393.14.9.14.9.

[8] Goldak J., Chakravarti A. and Bibby M., 1984. A new finite element model for welding heat sources. Metallurgical Tranactions B, Vol. 15B, P. 299-305. doi: 10.1007/BF02667333.

[9] Kazemi, M., 2021. Investigation of the effect of welding path on residual stresses and deformations in peripheral welding of steel pipe. Amirkabir Journal of Mechanical Engineering. 53:641-644. doi: 10.22060/mej.2020.18166.6752.

[10] Baharin, A., Yousef, H. and Bernd, M. 2022. Residual stresses in gas tungsten arc welding: a novel phase-field thermo-elastoplasticity modeling and parameter treatment framework. Computational Mechanics. 69:565-587. doi: 10.1007/s00466-021-02104-3.

[11] Sharyari, Z. Laribaghal, M. and Gheysari, K. 2023. Finite Element Simulation of Temperature Field and Residual Stress Induced by Surface Welding Process of Mild Steel. Journal of Manufacturing Innovations. 1:37-51. doi:10.22055/jomi.2024.39850.1005.